NJC

ROYAL SOCIETY OF CHEMISTRY

COMMUNICATION

View Article Online
View Journal | View Issue

Cite this: *New J. Chem.*, 2025, **49**, 16909

Received 8th July 2025,
Accepted 9th September 2025

DOI: 10.1039/d5nj02774h

rsc.li/njc

Preparation and photothermal properties of bio-inspired *Hydrangea*-like silica-alumina oxide microspheres

Rui Sun,[ab] Yuzhi Zhang,*[ab] Xinyu Wang,[a] Hongyu Gu,[a] Binghao Wang,[a] Jiaqi Wang,[ab] Yunsong Zhao,[ab] Xinchang Han,[ab] Jiayu Ma[a] and Lixin Song[ab]

***Hydrangea*-like silica-alumina oxide microspheres (HSAOM), bio-inspired by *Hydrangea* flowers, show excellent photothermal properties, achieving 90% solar reflectance and 97% atmospheric window emissivity. With their corrugated surface and hollow structure, HSAOM facilitated multifaceted light-regulation mechanisms, demonstrating potential for radiative cooling materials.**

Rising global energy demand and extreme climate events necessitate zero-energy cooling technologies. Passive radiative cooling (PRC) addresses this by exploiting the Earth's 8–13 μm atmospheric window.[1,2] Effective PRC materials require near-unity thermal emittance in this window and high solar reflectance (0.3–2.5 μm)—demanding specific micro–nano structures and chemical compositions.[3–6] From a micro–nano structural perspective, precisely ordered photonic crystal structures can significantly enhance solar reflection, while constructing scattering centres (*e.g.*, Mie scattering or Rayleigh scattering) across multiple length scales also effectively boosts solar reflectance, which concurrently facilitates infrared emission.[7,8] Regarding material composition, inorganic oxides like silicon dioxide (SiO_2) or aluminium oxide (Al_2O_3) are ideal: SiO_2 offers strong mid-infrared emission *via* phonon polaritons, while Al_2O_3 provides stability and ultraviolet resistance.[9–12] Silica-alumina composites, exemplified by Li *et al.*'s[13] nanofibrous aerogels demonstrating 90% solar reflectance and 97% window emittance, are thus highly promising for scalable PRC applications.[14–16]

Despite progress in engineered micro–nano radiative cooling materials, their optimization and scale-up face challenges like complex processing, high cost, and limited durability. Natural evolution offers inspiration, having produced complex structures that efficiently manage light and heat.[17–19] Bio-inspired radiative cooling materials mimic these multi-scale structures, achieving superior optical performance through simpler, eco-friendly methods.[20–22] For example, the Saharan silver ant's triangular hair-like structures scatter sunlight and enhance mid-infrared emission,[23] while the white beetle's disordered chitinous fiber network achieves near-perfect diffuse solar reflectance—principles transferable to material design.[24]

Hydrangea petal structures suggest ideas for PRC design. Their inflorescences form multi-scale corrugated surfaces (10–30 cm in diameter) through densely clustered small flowers.[25] This morphology enhances light scattering, reduces solar absorption, and enables the upper petals to shade the lower ones, mitigating heat accumulation.[26,27] Consequently, researchers are developing *Hydrangea*-like materials.[28–30] Examples include Wang *et al.*'s[31] *Hydrangea*-like MoS_2-modified kapok fibers enhancing electromagnetic wave scattering, and Chang *et al.*'s[32] *Hydrangea*-like TiO_2 structures boosting performance in photoelectric devices. Overall, this work aims to construct silica-alumina oxides featuring both surface corrugations and internal hollow structures inspired by *Hydrangea*. By leveraging these dual characteristics, surface corrugations and internal hollowness can be used to elevate reflectance in the ultraviolet–visible–near-infrared (UV-vis-NIR) and emissivity in the atmospheric transparent window. In addition, by exploring their photothermal properties, we seek to pioneer a novel pathway for next-generation radiative cooling materials characterized by high efficiency, low cost, and robust environmental adaptability.

The spherical aggregation of densely clustered small flowers in *Hydrangea* results in a characteristic corrugated surface and an inherently hollow structure (Fig. 1a). Our objective is to synthesize *Hydrangea*-like silica-alumina oxide microspheres, named HSAOM. The fabrication of HSAOM involves a two-step process: first, obtaining acidic octacarboxyl polyhedral oligomeric silsesquioxane (OCP) *via* the addition reaction of octavinyl polyhedral oligomeric silsesquioxane (OVP) and 3-mercaptopropionic acid (MPA); subsequently, HSAOM is produced through a solvothermal reaction between OCP and aluminium ions (Fig. S1, SI). The detailed synthesis procedure is

[a] *Research Center of Inorganic Coating Materials, Shanghai Institute of Ceramics, Chinese Academy of Sciences, Shanghai 201899, China. E-mail: yzzhang@mail.sic.ac.cn*

[b] *Center of Materials Science and Optoelectronics Engineering, University of Chinese Academy of Sciences, Beijing 100049, China*

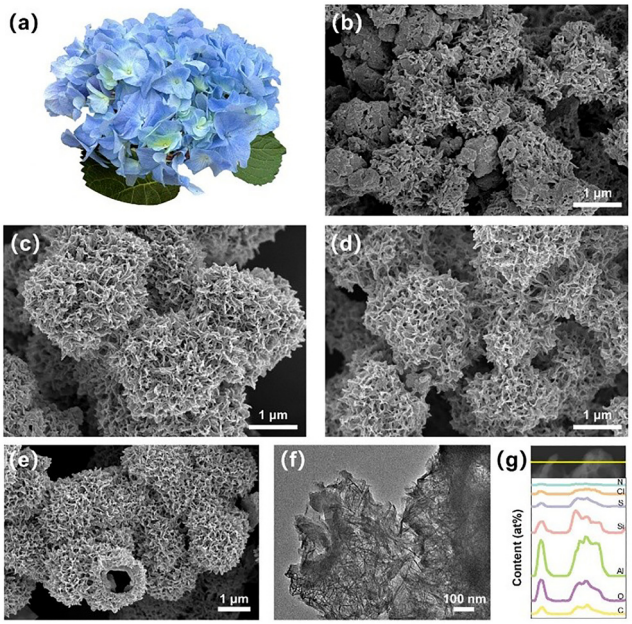

Fig. 1 (a) Image of *Hydrangea*. (b)–(d) SEM images of HSAOM 1# (b), HSAOM 2# (c) and HSAOM 3# (d). (e) SEM image, (f) TEM image and (g) EDS of fractured HSAOM.

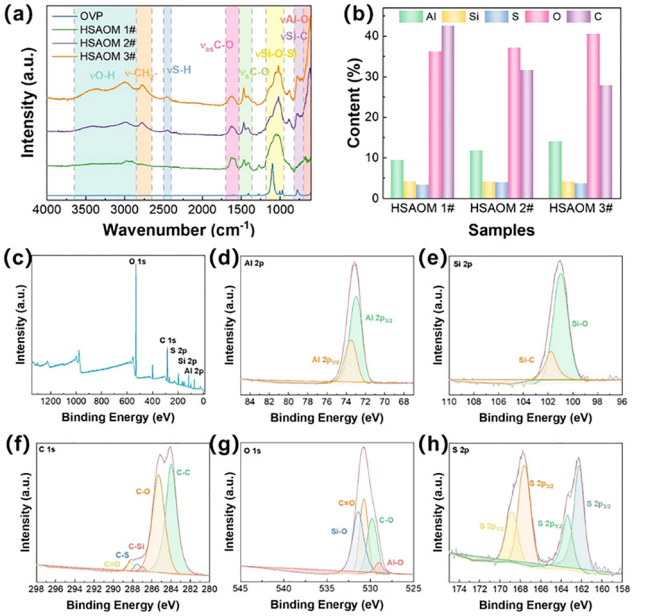

Fig. 2 (a) ATR-IR pattern and (b) element contents obtained by XPS of HSAOM. (c)–(h) XPS spectra of survey of HSAOM (c), Al 2p (d), Si 2p (d), C 1s (f), O 1s (g) and S 2p (h).

comprehensively described in the SI, with the three prepared HSAOM samples differing solely in the stoichiometric ratios of the reactants. Fig. 1 presents the microstructural characterization of the synthesized HSAOM. As shown in Fig. 1b–d, HSAOM is manifested as spherical microparticles (~1.5 μm in diameter) exhibiting a distinctive corrugated surface morphology. Complementary EDS analysis (Fig. S2, SI) confirmed a uniform elemental distribution throughout the HSAOM particles, verifying their successful preparation. The homogeneous corrugated features across the HSAOM surface demonstrate effective biomimicry of the structural topology of *Hydrangea*. Furthermore, examination of the HSAOM SEM image in Fig. 1e reveals a hollow spherical morphology, confirming the successful replication of another feature of *Hydrangea*. Therefore, the HSAOM material has been successfully synthesized.

TEM-EDS mapping of fractured HSAOM (Fig. 1f–g) revealed a uniform elemental distribution across the corrugated regions. Comparative EDS analysis (Table S1, SI) showed Al/Si enrichment within corrugations while maintaining consistent atomic ratios, indicating coordination-driven assembly between aluminium ions and OCP. HSAOM 1# exhibited fewer corrugations due to the lower Al content in the reactants, reducing aluminium ions and OCP coordination and altering the morphology. All samples maintained elemental uniformity, confirming the successful solvothermal synthesis of *Hydrangea*-like structures.

To further confirm bonding between aluminium ions and OCP, HSAOM was characterized using ATR-IR and XPS. The expected HSAOM with the target chemical composition is shown in Fig S1, SI; consequently, characterization for specific Si–O–Si and Al–O functional groups is necessary. ATR-IR (Fig. 2a) showed characteristic OVP peaks (νSi–O–Si: 1055 cm^{-1}; νSi–C: 782 cm^{-1}), confirming the retained siloxane cage structure. The symmetric and asymmetric stretching vibrations of C–O bonds at 1469 cm^{-1} and 1618 cm^{-1} indicated the successful progression of the addition reaction. Crucially, the intensity of the νAl–O peak increased with reactant Al content, demonstrating the formation of an Al–O bond. Concurrently, XPS results (Fig. 2d) provided additional confirmation of bonding between aluminium ions and OCP. The Si 2p, C 1s, and O 1s spectra of HSAOM (Fig. 2e–g) confirmed that the cage structure of siloxane remained intact, consistent with the target structural formula. Elemental analysis (Fig. 1b) revealed rising Al and O content in HSAOM with higher Al loading, providing direct evidence of the incorporation of Al–O and synthesis of the target oxide. These results collectively confirm the reaction between aluminium ions and OCP, although the precise structural formula requires further study.

Therefore, XRD was utilized for further investigation of the chemical composition. As shown in Fig. 3a, HSAOM exhibited no distinct characteristic peaks compared to OVP, indicating an amorphous state. However, based on the target chemical formula (Fig. S1, SI), complete bonding between aluminium ions and OCP was expected to yield a repeating unit with a relatively ordered structure, analogous to a metal organic framework. Consequently, HSAOM should not theoretically have been amorphous. To probe this further, we characterized the chemical composition of HSAOM using MALDI-TOF MS. Taking HSAOM 1# as an example, mass spectrometry analysis (Fig. 3b) revealed a relative molecular mass of 1274 Da for HSAOM 1#, with the closest matching chemical formula being $C_{22}H_{34}Al_{16}O_{16}S_2Si_8$. Comparing this to the target formula from OCP ($C_{40}H_{64}O_{28}S_8Si_8$, Fig. S1, SI), it was inferred that the addition reaction converting OVP to OCP did not proceed to completion. This incomplete addition of carboxyl groups

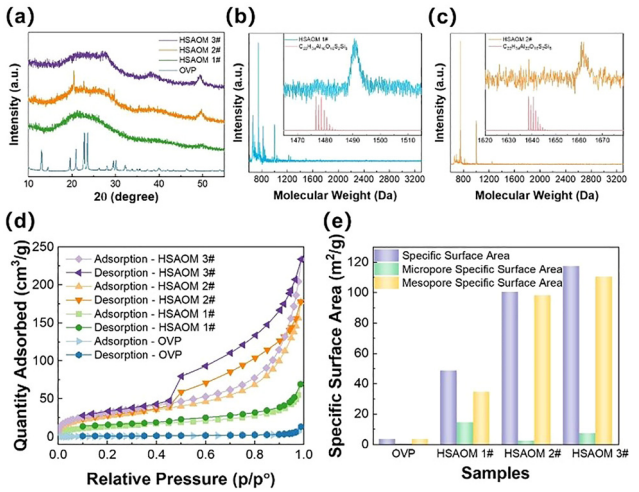

Fig. 3 (a) XRD pattern (b) and (c) MALDI-TOF MS pattern, (c) N_2 adsorption isotherms, (d) specific surface area of HSAOM.

resulted in either the addition occurring at random positions on the same OVP molecule or random OVP molecules being incompletely functionalized. This indeterminacy in the carboxyl group positions consequently led to indeterminate coordination sites for aluminium ions. Therefore, HSAOM adopted a disordered structure rather than a crystalline one, corroborating the XRD findings. Comparison of the MALDI-TOF MS results for different HSAOM samples (Fig. 3c and Fig. S3, SI) showed that HSAOM 2# had a higher relative molecular mass of 1436 Da compared to HSAOM 1#. This increase stemmed from the higher aluminium content in the reactants, leading to a greater aluminium content in the product. The corresponding chemical formula for HSAOM 2# was $C_{22}H_{34}Al_{22}O_{16}S_2Si_8$, where the stoichiometric ratio of Al to Si closely matched the ratio determined by XPS characterization in Fig. 2b. This further confirmed the increased aluminium coordination in HSAOM 2# compared to that in HSAOM 1#.

Upon determining the chemical composition of HSAOM, further characterization of its structural features was required. The porosity of HSAOM, characterized *via* BET analysis, provided an effective means to analyse its structure. As shown in Fig. 3d, HSAOM exhibits a significantly high specific surface area. The specific surface areas of OVP, HSAOM 1#, HSAOM 2#, and HSAOM 3# were 3.22 $m^2\ g^{-1}$, 48.57 $m^2\ g^{-1}$, 100.22 $m^2\ g^{-1}$, and 117.32 $m^2\ g^{-1}$, respectively. Compared to OVP, HSAOM formed by the coordination between aluminium ions and OCP demonstrated a substantial increase in specific surface area, which is also shown in Table S2, SI. Furthermore, the adsorption isotherm indicated the presence of both micropores and mesopores within the HSAOM structure. Based on its morphology (Fig. 1) and compositional characteristics (Fig. 2), it can be inferred that the mesopores originate primarily from the hollow microsphere structure formed by the coordination of aluminium ions with OCP, coupled with the corrugated surface morphology. Concurrently, the inherent cage-like structure of siloxane was preserved. These combined factors contributed to the exceptionally high specific surface area of HSAOM. HSAOM 2# exhibited a larger specific surface area than HSAOM 1#, attributable to increased aluminium coordination leading to enhanced surface corrugation, which further increased the specific surface area. The specific surface area of HSAOM 3# is comparable to that of HSAOM2#, which was also consistent with its microscopic morphology and chemical composition, indicating that the aluminium coordination sites approach saturation. This also indicates that the coordination of aluminium ions in 1# is unsaturated.

Following characterization of the microscopic morphology and chemical composition of HSAOM, it was confirmed that the synthesized HSAOM exhibited the anticipated features: a *Hydrangea*-like corrugated surface morphology and a hollow microsphere structure. Theoretically, HSAOM was expected to possess excellent photothermal properties. Consequently, the atmospheric window emissivity and solar reflectance of HSAOM were characterized *via* the equations in SI. As shown in Fig. 4a, HSAOM 1#, HSAOM 2#, and HSAOM 3# exhibited solar reflectance values of 91.35%, 89.04%, and 88.99%, respectively. Their atmospheric transparent window (8–13 μm) emissivity values were 97.02%, 97.41%, and 97.03%, respectively. HSAOM comprised hollow microspheres with a "*Hydrangea*-like" corrugated surface morphology, with a particle size of approximately 1–2 μm. Therefore, the micron-scale size of the microspheres effectively enhanced Mie scattering in the near-infrared (NIR) region, which can be proved by the increase in solar reflectance compared with OVP in Fig. S4, SI. Concurrently, the alteration in light propagation direction induced by the surface corrugations ensured high light scattering within the visible spectrum. These combined effects resulted in the high solar reflectance observed in HSAOM. As the primary chemical constituents of HSAOM were silica-alumina oxides, it inherently possessed high emissivity in the mid-to-far-infrared (MIR-FIR) region. Furthermore, the hollow microsphere structure facilitated multiple internal reflections and transmissions of light. This specific structure promoted the efficient dissipation of heat from the interior *via* radiation. The increased effective surface area

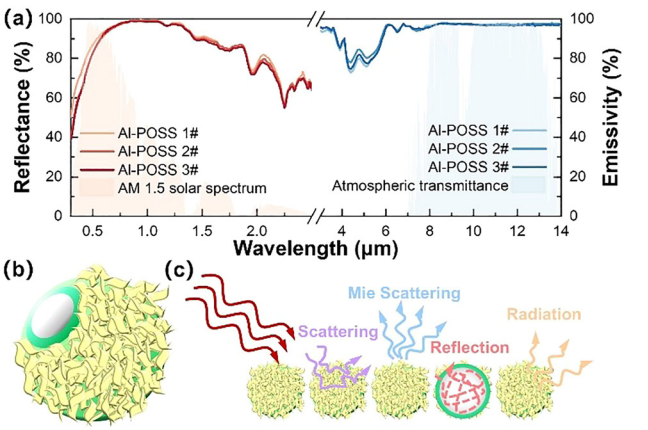

Fig. 4 (a) Reflectance and emissivity of HSAOM, AM 1.5 solar spectrum and atmospheric transmittance. (b) and (c) Schematic diagram of HSAOM (b) and the mechanism of photothermal properties (c).

provided by the corrugated morphology additionally enhanced thermal radiative emission capability. Consequently, HSAOM demonstrated high atmospheric transparent window emissivity (Fig. 4c). Considering the excellent solar reflectance and high atmospheric transparent window emissivity exhibited by HSAOM, the excellent photothermal properties of the material demonstrated significant potential for radiative cooling applications. This performance stemmed from the dual regulation achieved through its tailored chemical composition and optimized microstructure.

In summary, inspired by the characteristic surface corrugations and internal hollow structure of *Hydrangea* flowers, *Hydrangea*-like silica-alumina oxide hollow microspheres (HSAOM) were successfully synthesized *via* a two-step synthetic approach, involving an addition reaction followed by a solvothermal reaction. This process enabled coordination bonding between aluminium ions and OCP. Characterization of the HSAOM chemical composition confirmed the presence of characteristic peaks corresponding to siloxane and Al–O bonds, confirming successful coordination and formation of HSAOM. The chemical formula of HSAOM was determined. Analysis revealed the presence of indeterminate coordination sites attributed to incomplete addition reactions, which accounted for the amorphous structure of HSAOM. The synthesized HSAOM exhibited the targeted features of a corrugated surface and an internal hollow cavity, effectively mimicking the morphology of *Hydrangea* flowers. Crucially, this unique corrugated and hollow microstructure endowed HSAOM with a significantly high specific surface area. This substantial specific surface area, afforded primarily by the surface corrugations, enhances light scattering capabilities and improves photothermal properties. Concurrently, the micron-scale particle size of HSAOM effectively promoted Mie scattering, while the internal hollow structure facilitated multiple internal reflections, thereby augmenting radiative heat dissipation. Consequently, through the synergistic effects of scattering, Mie scattering, reflection, and radiation, HSAOM demonstrated high solar reflectance and high atmospheric transparent window emissivity. These combined characteristics underscore the excellent photothermal properties of HSAOM and its significant potential for radiative cooling applications, offering a novel strategy for the exploration of novel radiative cooling materials.

Conflicts of interest

There are no conflicts to declare.

Data availability

All data supporting this research are included in the main article and/or supplementary information (SI). Supplementary information: experimental section and supporting figures and tables. See DOI: **https://doi.org/10.1039/d5nj02774h**.

Acknowledgements

This work was supported by the National Natural Science Foundation of China (U22B20128) and the China Scientific Experiment Project (KJZ-YY-WCL401).

Notes and references

1 R. W. Bliss, *Sol. Energy*, 1961, **5**, 103–120.
2 S. Catalanotti, V. Cuomo, G. Piro, D. Ruggi, V. Silvestrini and G. Troise, *Sol. Energy*, 1975, **17**, 83–89.
3 Z. Ding, X. Li, Q. Ji, Y. Zhang, H. Li, H. Zhang, L. Pattelli, Y. Li, H. Xu and J. Zhao, *ACS Mater. Lett.*, 2024, **6**, 2416–2424.
4 Z. Ding, L. Pattelli, H. Xu, W. Sun, X. Li, L. Pan, J. Zhao, C. Wang, X. Zhang, Y. Song, J. Qiu, Y. Li and R. Yang, *Small*, 2022, **18**, 1–9.
5 B. Orel, M. K. Gunde and A. Krainer, *Sol. Energy*, 1993, **50**, 477–482.
6 L. Chen, K. Zhang, M. Ma, S. Tang, F. Li and X. Niu, *Build. Simul.*, 2020, **13**, 1165–1189.
7 W. Li, Y. Shi, Z. Chen and S. Fan, *Nat. Commun.*, 2018, **9**, 1–8.
8 J. Shang, J. Zhang, Y. Zhang, X. Zhang and Q. An, *Nano Lett.*, 2024, **24**, 7055–7062.
9 S. R. Wu, K. L. Lai and C. M. Wang, *Sci. Rep.*, 2018, **8**, 1–6.
10 G. Chen, Z. Zheng and P. Zhang, *Mater. Lett.*, 2025, **393**, 138560.
11 X. Ao, B. Li, B. Zhao, M. Hu, H. Ren, H. Yang, J. Liu, J. Cao, J. Feng, Y. Yang, Z. Qi, L. Li, C. Zou and G. Pei, *Proc. Natl. Acad. Sci. U. S. A.*, 2022, **119**, 1–7.
12 M. Li, C. Lin, K. Li, W. Ma, B. Dopphoopha, Y. Li and B. Huang, *Small*, 2023, **19**, 1–10.
13 T. Li, H. Sun, M. Yang, C. Zhang, S. Lv, B. Li, L. Chen and D. Sun, *Chem. Eng. J.*, 2023, **452**, 139518.
14 P. Lu, *Polym. Compos.*, 2025, 1–14.
15 D. Thiyagarajan, S. Li and B. K. Lee, *Nano Lett.*, 2025, **25**, 5609–5615.
16 Q. K. Xue, B. Wu, P. Luo, B. B. Li, G. L. Zhang, Y. B. Xue, H. J. Liu, Y. H. Yang, J. Kong, M. Zheng and Z. S. Wang, *Appl. Surf. Sci.*, 2025, **698**, 163047.
17 H. Zhou, T. Fan and D. Zhang, *ChemSusChem*, 2011, **4**, 1344–1387.
18 W. Fan, W. Bu and J. Shi, *Adv. Mater.*, 2016, **28**, 3987–4011.
19 H. Zhou, J. Xu, X. Liu, H. Zhang, D. Wang, Z. Chen, D. Zhang and T. Fan, *Adv. Funct. Mater.*, 2018, **28**, 1–27.
20 H. Zhou, L. Ding, T. Fan, J. Ding, D. Zhang and Q. Guo, *Appl. Catal., B*, 2014, **147**, 221–228.
21 R. H. Yang, S. An, W. Shang, T. Deng and W. Xuebao, *Acta Phys. Sin.*, 2022, **71**, 024401.
22 P. Zhou, Y. Wang and X. Zhang, *Nano Lett.*, 2024, **24**, 6395–6402.
23 N. N. Shi, C. C. Tsai, F. Camino, G. D. Bernard, N. Yu and R. Wehner, *Science*, 2015, **349**, 298–301.
24 D. Xie, Z. Yang, X. Liu, S. Cui, H. Zhou and T. Fan, *Soft Matter*, 2019, **15**, 4294–4300.
25 S. Kazaz, T. Kılıç, E. Doğan and Ş. Sekmen, *J. Hortic. Sci. Biotechnol.*, 2020, **95**, 325–330.
26 E. Kesumawati, M. Hosokawa, T. Kimata, T. Uemachi and S. Yazawa, *Sci. Hortic.*, 2009, **121**, 199–205.

27 Z. Li, T. Lyu and Y. Lyu, *Horticulturae*, 2024, **10**, 586.
28 H. M. A. Hassan, M. S. Alhumaimess, I. H. Alsohaimi, S. K. Mohamed, O. F. Aldosari, T. S. Alraddadi and A. A. Essawy, *Colloids Surf., A*, 2022, **654**, 130056.
29 F. Xie, Q. Wang, M. Gan and L. Ma, *New J. Chem.*, 2023, **48**, 646–653.
30 Y. Wu, J. Li, X. Zhang, C. Guo, Y. Fan, X. Cheng, Y. Xu, S. Gao and L. Huo, *Appl. Surf. Sci.*, 2023, **640**, 158381.
31 X. Wang, X. Cao, E. Ding, M. Yin, L. Huang and L. Zhang, *Carbon*, 2024, **221**, 118887.
32 W. C. Chang, B. H. Tang, Y. W. Lu, W. C. Yu, L. Y. Lin and R. J. Wu, *J. Power Sources*, 2016, **319**, 131–138.